Global stability analysis of the natural convection between two horizontal concentric cylinders

J.J. Serrano-Aguilera [a,*], Francisco J. Blanco-Rodríguez [b], L. Parras [a]

[a] Universidad de Málaga, Escuela de Ingenierías Industriales, Campus de Teatinos s/n, 29071, Málaga, Spain
[b] Área de Mecánica de Fluidos, Departamento de Ingeniería Aeroespacial y Mecánica de Fluidos, Universidad de Sevilla, Avenida de los Descubrimientos s/n, 41092, Sevilla, Spain

ARTICLE INFO

ABSTRACT

In this investigation, the 2D flow between two horizontally positioned concentric cylinders (gravity perpendicular to the axis of the cylinders), where the inner cylinder is kept at constant temperature T_i higher than the outer border temperature T_o, is analyzed. Buoyancy forces initiate the movement of the fluid and the generated flow is studied in a fixed geometry for values of Prandtl numbers (Pr) between 0.01 and 1, and Rayleigh numbers (Ra) between 10^2 and $5 \cdot 10^6$. To solve the problem, a Chebyshev-Fourier spectral code is developed in polar coordinates (r, θ) respectively, and a complete map of steady-state solutions is obtained where regions with multiple solutions are identified. Later, a global stability study of the obtained stationary solutions is carried out, providing a transition curve to unstable areas as a function of the control parameters of the problem (Pr, Ra). Finally, to check the stability results, temporal evolution simulations are accomplished for several cases where dual solutions are presented, finding intermediate almost stationary solutions, and demonstrating that there exist typically single oscillating plume or double oscillating plume solutions (depending on the parameter space), where some of them have higher heat transfer coefficients, which may be interesting alternatives to improve heat exchange systems by means of passive control techniques.

1. Introduction

Convection is a major feature of the dynamics of the oceans, the atmosphere, and the interior of stars and planets [1,2]. Natural convection systems often exhibit surprisingly regular large scale patterns. Examples are the solar granulation and mesoscale convection in the Earth's atmosphere as visualized by the cloud patterns seen in satellite images. Evidently, the presence of large-scale regular structures at extremely large Reynolds and Rayleigh numbers, often presumed in these systems to be asymptotically large, is compatible with a broad spectrum of highly chaotic motions at intermediate scales. Unfortunately, this aspect of turbulent convection cannot be easily investigated in laboratory experiments.

Fluid motion driven by thermal gradients (thermal convection) is a common and important phenomenon in nature. Due to its theoretical interest and its various engineering applications such as

heat exchangers, thermal energy storage systems, cooling of electronic components, transmission cables and solar thermal energy [3], natural convection heat transfer in a horizontal cylindrical annulus kept at constant surface temperature has been the subject of interest of many researchers. Its simple geometry and well-defined boundary conditions allow to characterize the phenomenon by two dimensionless parameters: the Prandtl number (Pr) which is the ratio of viscous diffusivity to thermal diffusivity and the Rayleigh number (Ra) which can be seen as the ratio of the gravitational potential energy to the energy due to viscous dissipation and thermal diffusion. The aspect ratio $A \equiv D_i/L$ which is the ratio of inner cylinder diameter D_i to the gap width L constitutes the last parameter of the problem.

Many fundamental aspects of patterns and their instabilities have been studied intensively over the past five decades in the context of Rayleigh-Bénard convection (RBC). In a traditional RBC experiment, a horizontal fluid layer of height d is confined between two thermally well conducting, parallel plates. When the difference $\Delta T = T_b - T_t$ between the bottom-plate temperature T_b and the top-plate temperature T_t exceeds a critical value ΔT_{crit}, the conductive motionless state is unstable and convection sets in. The

* Corresponding author.
E-mail addresses: jj.serragui@uma.es (J.J. Serrano-Aguilera), fbrodriguez@us.es (F.J. Blanco-Rodríguez), lparras@uma.es (L. Parras).

Nomenclature

A	aspect ratio
D	diameter (m)
J	Jacobian
L	gap width between cylinders (m)
Pr	Prandtl number
Ra	Rayleigh number
Nu	Nusselt number
T	temperature (K)
$\mathbf{A}$	differential operator
$\mathbf{B}$	differential operator
$\mathbf{f}$	generic function in the Newton-Raphson solver
$\mathbf{f}_m$	mass force (N·kg^{-1})
$\mathbf{q}$	solution column vector
$\mathbf{u}$	velocity field (m·s^{-1})
$\mathcal{R}$	cylinder radius ratio
d	layer height (m)
g	gravitational acceleration (m·s^{-2})
k	thermal conductivity (W·m^{-1}·K^{-1})
N	number of discretization nodes
p	pressure (Pa)
r	radial coordinate (m)
t	time (s)
u	radial component of velocity field (m·s^{-1})
v	azimuthal component of velocity field (m·s^{-1})

Abbreviations

CVFEM	control volume based finite element method
FDM	finite difference method
FEM	finite element method
FVM	finite volume method
KG	Kuehn & Goldstein
LBM	Lattice Boltzmann method
MPS	moving particle semi-implicit method
RBC	Rayleigh-Bénard convection
S	stable solution
SPH	smoothed particle hydrodynamics method
SU	dual stable-unstable solution
U	unstable solution
UU	dual unstable solution

Greek Symbols

α	thermal diffusivity (m^2·s^{-1})
β	thermal volumetric expansion coefficient (K^{-1})
ΔT	temperature difference (K)
ϵ	dimensionless distance
λ	complex eigenvalue in global stability analysis
λ_w	wavelength (m)
∇	differential operator nabla
ν	kinematic viscosity (m^2·s^{-1})
ω	vorticity (s^{-1})
ξ	Chebyshev discretization variable (radial coordinate)
Φ	temperature field with homogeneous boundary conditions (K)
Ψ	stream function (m^2·s^{-1})
ρ	density (kg·m^{-3})
θ	azimuthal coordinate

Subscripts

B	Boussinesq
BC	boundary conditions
b	bottom
c	characteristic
crit	critical

eq	equivalent
H	hydrostatic
i	inner, imaginary part
j	iteration index
m	marginal
max	maximum
o	outer
r	radial
s	steady
t	top
z	z-axis (perpendicular to $r-\theta$ domain)
θ	azimuthal

Superscripts

$'$	perturbation
$\hat{}$	dimensionless form
$-$	average
T	transpose

simplest pattern which can occur is that of straight, parallel convection rolls with a horizontal wavelength $\lambda_w \approx 2\,d$ (wave number $\kappa \approx \pi/d$). Such rolls can be found near onset; however, as the dimensionless distance $\epsilon \equiv \Delta T/\Delta T_{crit} - 1$ increases, the patterns often become progressively more complicated, and thus also more interesting. In their attempts to reach high Rayleigh numbers Ra, experimental researches have focused on convection layers with small aspect ratios (horizontal width to height) which do not permit the realizations of spontaneous large-scale patterns in highly turbulent convection. In fact, typical high Rayleigh number experiments are carried out with an aspect ratio of the order unity or less [4,5]. RBC is perhaps the most thoroughly investigated and understood pattern-forming system. The experimental setup is simple in principle and the basic physical mechanism (buoyancy vs dissipation), which can be described in terms of the Oberbeck-Boussinesq equations, is well understood.

The basic flow field from the natural convection heat transfer in a horizontal cylindrical annulus for low value of Ra consists of two symmetric crescent-shaped eddies in which fluid rises near the inner hotter cylinder and sinks near the outer colder one. At high Ra, however, several kinds of convective flows which are dependent on Pr and aspect ratio A can be developed. According to Kuehn and Goldstein [6], the flow in a horizontal cylindrical annulus is steady over the range of Rayleigh number from 10^2 to 10^5. Kuehn and Goldstein [7] also experimentally studied the flow patterns at Rayleigh numbers from $2.2 \cdot 10^2$ to $7.7 \cdot 10^7$, and they found that the plume above the inner cylinder began to oscillate when Rayleigh number was near $2 \cdot 10^5$ and the entire plume was turbulent at $Ra \approx 2 \cdot 10^6$. Their results also showed that the local heat transfer coefficient depended significantly on the eccentricity while the overall heat transfer coefficients changed by less than 10% with the change of eccentricity. Yoo [8] in his outstanding work, reported the occurrences of dual solutions at Ra larger than a critical value. Using a vorticity-streamfunction formulation, he observed dual steady solutions at $Ra > Ra_{crit} \approx 3800$ for wide gap annuli ($A = 2$). Similar results were provided later by Mizushima and Hayashi [9], Mizushima et al. [10], Xin and Le Quéré [11] and Mercader et al. [12]. After the emergence of the nanofluids that have been shown to improve heat transfer process effectively, numerous research works have been also devoted to study heat transfer improvement in annuli systems using nanofluids [13,14].

In the last decades, a considerable amount of effort has been dedicated to study natural convection instabilities and bifurcations in horizontal concentric annuli. Powe et al. [15] experimentally investigated the bifurcation of natural convection of air ($Pr = 0.7$) by visualizing flow patterns, and categorized the flow patterns ob-
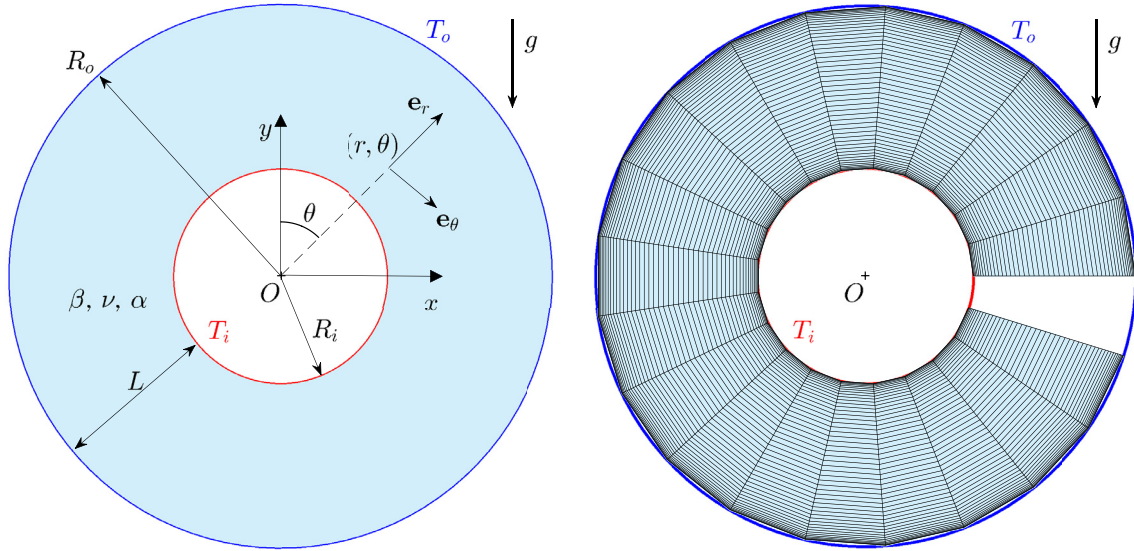
Fig. 1. Sketch (left) and computational grid (right) of the problem.

tained by their experiments and accumulated results by other researchers in a parameter space of $(Ra, \mathcal{R})$ where $\mathcal{R} \equiv R_o/R_i = 1 + (2/A)$ is the cylinder radius ratio. This experiment was repeated and the classification was confirmed by Dyko et al. [16]. Busse [1] discussed the non-linear properties such as the dependence of the heat transport on Rayleigh and Prandtl numbers and the stability properties of thermal convection. Janssen and Henkes [17] analyzed the instabilities in three dimensional differentially-heated cavities with adiabatic horizontal walls. Petrone et al. [18] performed a stability analysis of numerical steady-state solutions, and provided a detail of the bifurcation diagram near the imperfect bifurcation for different radius ratio $\mathcal{R} = 1.2, 1.4$ and 2 at $Pr = 0.7$. Angeli et al. [19] provided a critical review of buoyancy-induced flow transitions in horizontal annuli. Soucasse et al. [20] studied the transitional regimes of natural convection in a differentially heated cubical cavity under the effects of wall and molecular gas radiation. Other well-known instability of the convective flows is the flickering instability [21,22].

In the present research work an extensive numerical analysis has been implemented in order to obtain a complete steady-state solution $Pr - Ra$ map for a fixed aspect ratio of $A = 1.25$. Furthermore, a global stability analysis has been also performed and the marginal stability curve $Ra_{crit} = f(Pr)$ has been obtained. Different regions with dual solutions have been identified and it is shown that in the unstable region the solution always reaches an attractor that appears as a vertical oscillating plume which is anchored to the inner cylinder and whose spatial and temporal structure can be explained through the flickering instability [21], although its development is very limited by the upper surface.

2. Governing equations

The problem of buoyancy (gravitational) induced motion of a fluid in a two-dimensional annulus is formulated using the Boussinesq approximation to solve the governing equations of mass, momentum and energy. Note that in the Boussinesq approximation, density variations are assumed to have a fixed part and another part that has a linear dependence on temperature:

$$\rho_B(T) = \rho[1 - \beta(T - T_o)], \tag{1}$$

where T is the temperature at a point within the fluid, β the thermal volumetric expansion coefficient and T_o is the temperature of

the outer cylinder. Fig. 1 shows the geometry of the problem along with the polar coordinate system adopted in which the radial coordinate r is measured from the center of the system and θ is measured clockwise from the upward vertical line. Moreover, the radial velocity u is positive radially outwards and the angular velocity v is positive in the clockwise direction.

The governing equations for the natural convection in the region between horizontal concentric cylinders for an incompressible fluid can be written as

$$\nabla \cdot \mathbf{u} = \mathbf{0}, \tag{2}$$

$$\frac{D\mathbf{u}}{Dt} = -\frac{1}{\rho} \nabla p + \nu \nabla^2 \mathbf{u} + \frac{\rho_B(T)}{\rho} \mathbf{f}_m, \tag{3}$$

$$\frac{DT}{Dt} = -\alpha \nabla^2 T. \tag{4}$$

where ν is the kinematic viscosity, α is the thermal diffusivity, $\mathbf{u} = u(r, \theta)\mathbf{e}_r + v(r, \theta)\mathbf{e}_\theta$, $\frac{D}{Dt} \equiv \frac{\partial}{\partial t} + \mathbf{u} \cdot \nabla$ is the material derivative and $\mathbf{f}_m$ is the body force per unit mass which corresponds with gravity field for the case the annulus is not rotating.

For the situation in which the fluid is quiescent ($\mathbf{u} = \mathbf{0}$) and at uniform temperature the above equations simplify as

$$-\nabla p_H + \rho \, \mathbf{f}_m = \mathbf{0}. \tag{5}$$

Eq. (5) reveals that we can redefine the pressure as $p^* = p - p_H$ and the linear momentum equation can be written as

$$\frac{D\mathbf{u}}{Dt} = -\frac{1}{\rho} \nabla p^* + \nu \nabla^2 \mathbf{u} + g\beta(T - T_o) \, \mathbf{e}_y, \tag{6}$$

where $\mathbf{f}_m = -g\mathbf{e}_y$. According to the Fig. 1, the linear momentum equation can be written in polar coordinates as

$$\frac{D\mathbf{u}}{Dt} = -\frac{1}{\rho} \nabla p^* + \nu \nabla^2 \mathbf{u} + g\beta(T - T_o)(\cos\theta \mathbf{e}_r - \sin\theta \mathbf{e}_\theta), \tag{7}$$

The equations governing the phenomenon should also be deduced from the stream function-vorticity ($\Psi - \omega$) formulation. The velocity field is given as

$$\mathbf{u} = \frac{1}{r} \frac{\partial \Psi}{\partial \theta} \, \mathbf{e}_r - \frac{\partial \Psi}{\partial r} \, \mathbf{e}_\theta, \tag{8}$$

which automatically fulfils the incompressible constraint. The vorticity field for the resulting 2D problem has only one component perpendicular to the problem sketch as $\boldsymbol{\omega} = \omega\,\mathbf{e}_z$ which is given by

$$\omega = (\nabla \times \mathbf{u}) \cdot \mathbf{e}_z = \nabla^2 \Psi, \tag{9}$$

Taking the curl of Eq. (7) and projecting onto the z-axis, the vorticity equation is obtained as

$$\frac{D\omega}{Dt} = \nu\,\nabla^2\omega + g\,\beta\left[\frac{1}{r}\cos\theta\,\frac{\partial}{\partial\theta}(T - T_o) + \sin\theta\,\frac{\partial}{\partial r}(T - T_o)\right]. \tag{10}$$

Furthermore, by setting the characteristic time and length of the problem as $t_c = \frac{L^2}{\alpha}$ and $l_c = L = R_o - R_i$, respectively

$$\frac{D}{Dt} \equiv \frac{\alpha}{L^2}\frac{D}{D\hat{t}}, \quad \nabla^2 \equiv \frac{1}{L^2}\hat{\nabla}^2, \quad \hat{T} = \frac{T - T_o}{T_i - T_o}, \quad r = L\hat{r}, \quad \omega = \frac{\alpha}{L^2}\hat{\omega},$$
$$\Psi = \alpha\hat{\Psi} \tag{11}$$

the non-dimensional equations that govern the problem are:

$$\hat{\omega} = \hat{\nabla}^2\hat{\Psi}, \tag{12}$$

$$\frac{1}{Pr}\frac{D\hat{\omega}}{D\hat{t}} = \hat{\nabla}^2\hat{\omega} + Ra\left[\frac{1}{\hat{r}}\cos\theta\,\frac{\partial\hat{T}}{\partial\theta} + \sin\theta\,\frac{\partial\hat{T}}{\partial\hat{r}}\right], \tag{13}$$

$$\frac{D\hat{T}}{D\hat{t}} = \hat{\nabla}^2\hat{T}. \tag{14}$$

where $Pr = \frac{\nu}{\alpha}$ and $Ra = \frac{g\,\beta\,L^3\,(T_i - T_o)}{\nu\,\alpha}$ are the Prandtl and Rayleigh numbers, respectively.

If we change the convention of sign of the vorticity ($\omega \to -\omega$) and use the free-fall velocity $V_f = \sqrt{g\,L\,\beta\,(T_i - T_o)}$ instead of α/L as a characteristic velocity for scaling the velocity then the governing equations read

$$\hat{\omega} = -\hat{\nabla}^2\hat{\Psi}, \tag{15}$$

$$\frac{D\hat{\omega}}{D\hat{t}} = \sqrt{\frac{Pr}{Ra}}\hat{\nabla}^2\hat{\omega} - \left[\frac{1}{\hat{r}}\cos\theta\,\frac{\partial\hat{T}}{\partial\theta} + \sin\theta\,\frac{\partial\hat{T}}{\partial\hat{r}}\right], \tag{16}$$

$$\frac{D\hat{T}}{D\hat{t}} = \frac{1}{\sqrt{Pr\,Ra}}\hat{\nabla}^2\hat{T}, \tag{17}$$

which are the equations we have solved in the present work and coincide with those appearing in [23].

The bi-harmonic equation for the streamfunction $\hat{\Psi}$ is given by

$$\frac{\partial\hat{\nabla}^2\hat{\Psi}}{\partial\hat{t}} + J\left(\hat{\nabla}^2\hat{\Psi}, \hat{\Psi}\right) = \sqrt{\frac{Pr}{Ra}}\hat{\nabla}^4\hat{\Psi} + \left[\frac{1}{\hat{r}}\cos\theta\,\frac{\partial\hat{T}}{\partial\theta} + \sin\theta\,\frac{\partial\hat{T}}{\partial\hat{r}}\right], \tag{18}$$

$$\frac{\partial\hat{T}}{\partial\hat{t}} + J(\hat{T}, \hat{\Psi}) = \frac{1}{\sqrt{Pr\,Ra}}\hat{\nabla}^2\hat{T}. \tag{19}$$

where $J(\eta, \hat{\Psi}) \equiv \frac{1}{\hat{r}}\left(\frac{\partial\hat{\Psi}}{\partial\theta}\frac{\partial\eta}{\partial\hat{r}} - \frac{\partial\hat{\Psi}}{\partial\hat{r}}\frac{\partial\eta}{\partial\theta}\right)$ represents the convective term.

The boundary conditions on the two impermeable isothermal walls are given by

$$\hat{\Psi} = \frac{\partial\hat{\Psi}}{\partial\hat{r}} = 0, \quad \hat{T} = 1, \tag{20}$$

on the inner cylinder ($\hat{r} = R_i/L$) and

$$\hat{\Psi} = \frac{\partial\hat{\Psi}}{\partial\hat{r}} = 0, \quad \hat{T} = 0, \tag{21}$$

on the outer cylinder ($\hat{r} = R_o/L$).

In case symmetry with respect to the y axis is imposed, where only half of the annulus is taken as the computational domain, the following symmetric condition is applied along two vertical lines of symmetry at $\theta = 0$ and $\theta = \pi$:

$$\hat{\Psi} = \frac{\partial\hat{\Psi}}{\partial\theta} = \frac{\partial\hat{T}}{\partial\theta} = 0. \tag{22}$$

The solution of the heat equation with the same boundary conditions (which is only function of the radial coordinate) is an important reference to measure heat transfer efficiency of natural convection process. Therefore, in order to measure the convergence of the system and compare our solutions with those provided by other authors [6,24], the local and average equivalent conductivity [23,25] are defined as follows:

$$k_{eq}(\hat{r}, \theta) \equiv \frac{Nu}{Nu_c} = -\hat{r}\ln(\mathcal{R})\frac{\partial\hat{T}}{\partial n},$$
$$\bar{k}_{eq}(\hat{r}) \equiv \frac{\oint k_{eq}(\hat{r}, \theta)\,ds}{2\pi\,\hat{r}} = \frac{-\ln(\mathcal{R})}{2\pi}\oint\frac{\partial\hat{T}}{\partial n}\,ds, \tag{23}$$

where $Nu_c \equiv \frac{1}{\ln(\mathcal{R})}$ is the Nusselt number corresponding to the pure conductive flow and $\mathcal{R} = \frac{R_o}{R_i} = 1 + 2\frac{L}{D_i} = 1 + \frac{2}{A}$ is the radius ratio. According to the geometric configuration we are dealing with ($\frac{\partial\hat{T}}{\partial n} = \frac{\partial\hat{T}}{\partial r}$ and $ds = r\,d\theta$), the above equation can be further reduced to

$$\bar{k}_{eq,i} = \frac{-\ln(\mathcal{R})}{2\pi\,(\mathcal{R}-1)}\int_0^{2\pi}\frac{\partial\hat{T}}{\partial\hat{r}}\,d\theta. \tag{24}$$

for the inner cylinder ($\hat{r} = \frac{R_i}{L}$), and

$$\bar{k}_{eq,o} = \frac{-\mathcal{R}\,\ln(\mathcal{R})}{2\pi\,(\mathcal{R}-1)}\int_0^{2\pi}\frac{\partial\hat{T}}{\partial\hat{r}}\,d\theta. \tag{25}$$

for the outer cylinder ($\hat{r} = \frac{R_o}{L}$).

Fig. 2 shows the computational grid used for solving the problem where periodic boundary condition is employed in the azimuthal direction, θ. Additionally, Chebyshev discretization allows to radially concentrate the nodes near the walls ($\xi = \pm 1$) in order to accurately solving both the thermal and velocity boundary layers.

3. Numerical method

In recent years, a number of numerical methods have been applied to study natural convection in a horizontal cylindrical annulus, such as finite element method (FEM) [26,27], finite difference method (FDM) [28], finite volume method (FVM) [29,30], lattice Boltzmann method (LBM) [31,32], differential quadrature method [33], control volume based finite element method (CVFEM) [34], moving particle semi-implicit method (MPS) [35] and a smoothed particle hydrodynamics (SPH) method [36]. However, most of the previous studies did not consider the effect of the Prandtl number on the natural convection heat transfer in a horizontal cylindrical annulus. The objective of the present work is to extend our knowledge of flow patterns in a horizontal concentric annulus for a wide range of Rayleigh numbers (10^2 to $5 \cdot 10^6$) and Prandtl numbers (0.01 to 1).

We perform a spectral numerical method for the spatial variables using Chebyshev and Fourier discretizations for the radial and azimuthal variables, respectively. Boundary conditions are directly implemented in the derivation matrices using the DM suite toolbox [37]. The dimensionless radial domain ($\hat{r} \in [R_i/L, R_o/L]$) is mapped (see Fig. 2) in the Chebyshev domain ($\xi \in [-1, 1]$) using the following path

$$\hat{r} = \frac{1}{2}(\xi + 1) + \frac{R_i}{L} = \frac{1}{2}(\xi + 1) + \frac{A}{2} \quad \rightarrow \quad \xi = 2\hat{r} - (A + 1). \tag{26}$$
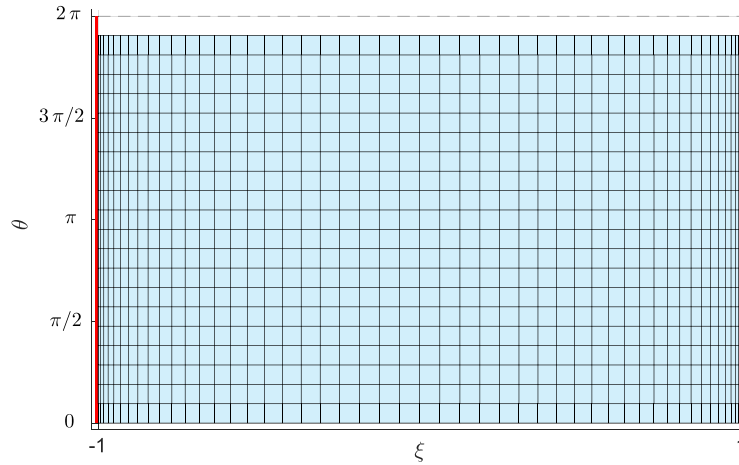
Fig. 2. Grid of the numerical domain.

Since the derivation matrices implemented in the DM suite require Dirichlet boundary conditions for the temperature, we have decomposed the temperature field as

$$\hat{T}(\hat{r}, \theta, \hat{t}) = \hat{\Phi}(\hat{r}, \theta, \hat{t}) + \hat{T}_{BC}(\hat{r}) = \hat{\Phi}(\hat{r}, \theta, \hat{t}) + \left(\frac{R_o}{L} - \hat{r}\right)$$

$$= \hat{\Phi}(\hat{r}, \theta, \hat{t}) + \left(1 + \frac{A}{2} - \hat{r}\right). \tag{27}$$

Substituting the above equation in the vorticity and temperature equations ((15)–(17)), we obtain

$$\hat{\omega} = -\hat{\nabla}^2\hat{\Psi}, \tag{28}$$

$$\frac{D\hat{\omega}}{D\hat{t}} = \sqrt{\frac{Pr}{Ra}}\hat{\nabla}^2\hat{\omega} - \left[\frac{1}{\hat{r}}\cos\theta\frac{\partial\hat{\Phi}}{\partial\theta} + \sin\theta\frac{\partial\hat{\Phi}}{\partial\hat{r}}\right] + \sin\theta, \tag{29}$$

$$\frac{D\hat{\Phi}}{D\hat{t}} - \frac{1}{\hat{r}}\frac{\partial\hat{\Psi}}{\partial\theta} = \frac{1}{\sqrt{Pr Ra}}\left(\hat{\nabla}^2\hat{\Phi} - \frac{1}{\hat{r}}\right). \tag{30}$$

The main advantage of the above formulation is that the deviatoric temperature field $\hat{\Phi}$, has homogeneous Dirichlet boundary conditions at both the inner ($\hat{r} = R_i/L$ or $\xi = -1$) and outer (R_o/L or $\xi = 1$) walls [38].

To reduce the size of the system to solve, the flow variables used are $\hat{\Psi}$ and $\hat{\Phi}$, and once defined the vector $\mathbf{q} = [\hat{\Psi}, \hat{\Phi}]^T$, the system of equations to solve can be written as

$$\mathbf{A}\frac{\partial\mathbf{q}}{\partial\hat{t}} = \mathbf{f}(\hat{t}, \mathbf{q}), \tag{31}$$

with

$$\mathbf{A} = \begin{pmatrix} \hat{\nabla}^2 & 0 \\ 0 & 1 \end{pmatrix}, \tag{32}$$

and

$$\mathbf{f}(\hat{t}, \mathbf{q}) = \begin{pmatrix} -\frac{1}{\hat{r}}\left(\frac{\partial\hat{\Psi}}{\partial\theta}\frac{\partial\hat{\nabla}^2\hat{\Psi}}{\partial\hat{r}} - \frac{\partial\hat{\Psi}}{\partial\hat{r}}\frac{\partial\hat{\nabla}^2\hat{\Psi}}{\partial\theta}\right) + \sqrt{\frac{Pr}{Ra}}\hat{\nabla}^4\hat{\Psi} \\ +\left[\frac{1}{\hat{r}}\cos\theta\frac{\partial\hat{\Phi}}{\partial\theta} + \sin\theta\left(\frac{\partial\hat{\Phi}}{\partial\hat{r}} - 1\right)\right] \\ -\frac{1}{\hat{r}}\left(\frac{\partial\hat{\Psi}}{\partial\theta}\frac{\partial\hat{\Phi}}{\partial\hat{r}} - \frac{\partial\hat{\Psi}}{\partial\hat{r}}\frac{\partial\hat{\Phi}}{\partial\theta}\right) + \frac{1}{\sqrt{Pr Ra}}\left(\hat{\nabla}^2\hat{\Phi} - \frac{1}{\hat{r}}\right) + \frac{1}{\hat{r}}\frac{\partial\hat{\Psi}}{\partial\theta} \end{pmatrix}. \tag{33}$$

3.1. Steady solver

To obtain the steady solution $[\hat{\Psi}_s, \hat{\Phi}_s]^T$ of Eq. (31), a Newton-Raphson solver has been implemented as

$$\mathbf{q}_{j+1} = \mathbf{q}_j - \left[\nabla_\mathbf{q}\mathbf{f}(\mathbf{q}_j)\right]^{-1}\mathbf{f}_j = \mathbf{q}_j - \left[\mathbf{B}(\mathbf{q}_j)\right]^{-1}\mathbf{f}_j, \tag{34}$$

where $\mathbf{f}_j = \mathbf{f}(\hat{t}, \mathbf{q}_j)$ and

$$\mathbf{B} \equiv \nabla_\mathbf{q}\mathbf{f} = \begin{pmatrix} -\frac{1}{\hat{r}}\left(\frac{\partial\hat{\Psi}_j}{\partial\theta}\frac{\partial\hat{\nabla}^2}{\partial\hat{r}} + \frac{\partial\hat{\nabla}^2\hat{\Psi}_j}{\partial\hat{r}}\frac{\partial}{\partial\theta} - \frac{\partial\hat{\Psi}_j}{\partial\hat{r}}\frac{\partial\hat{\nabla}^2}{\partial\theta} - \frac{\partial\hat{\nabla}^2\hat{\Psi}_j}{\partial\theta}\frac{\partial}{\partial\hat{r}}\right) \\ +\sqrt{\frac{Pr}{Ra}}\hat{\nabla}^4 \qquad \frac{1}{\hat{r}}\cos\theta\frac{\partial}{\partial\theta} + \sin\theta\frac{\partial}{\partial\hat{r}} \\ -\frac{1}{\hat{r}}\left(\frac{\partial\hat{\Phi}_j}{\partial\hat{r}}\frac{\partial}{\partial\theta} - \frac{\partial\hat{\Phi}_j}{\partial\theta}\frac{\partial}{\partial\hat{r}} - \frac{\partial}{\partial\theta}\right) \\ \qquad\qquad -\frac{1}{\hat{r}}\left(\frac{\partial\hat{\Psi}_j}{\partial\theta}\frac{\partial}{\partial\hat{r}} - \frac{\partial\hat{\Psi}_j}{\partial\hat{r}}\frac{\partial}{\partial\theta}\right) + \frac{1}{\sqrt{Pr Ra}}\hat{\nabla}^2 \end{pmatrix}, \tag{35}$$

and j marks the index for each iteration of the algorithm. It is worth mentioning that the steady solutions have been sought taking advantage of their symmetry (anti-symmetric $\hat{\Psi}_s$ and symmetric $\hat{\Phi}_s$) with respect to the vertical axis ($\theta = 0$). It has been implemented by means of folding the differentiation matrices, which has allowed a significant reduction of the required computing resources by solving only within the $\theta \in [0, \pi]$ range. A steady solution is considered converged if $\max(|\mathbf{f}_j|) < 10^{-8}$.

3.2. Unsteady solver

To solve the unsteady problem a 4th order Runge-Kutta method has been implemented in the full domain (i.e. symmetry has not been imposed) as it is described in [39]. Defining the time step as $\Delta\hat{t}$, the time evolution Eq. (31) are solved following the rule (where the superscript n defines the different time instants),

$$\mathbf{q}^{n+1} = \mathbf{q}^n + \mathbf{A}^{-1}\frac{1}{6}\Delta\hat{t}(\mathbf{k}_1 + 2\mathbf{k}_2 + 2\mathbf{k}_3 + \mathbf{k}_4), \tag{36}$$

with

$$\mathbf{k}_1 = \mathbf{f}(\hat{t}_n, \mathbf{q}^n), \tag{37}$$

$$\mathbf{k}_2 = \mathbf{f}(\hat{t}_n + \Delta\hat{t}/2, \mathbf{q}^n + \mathbf{k}_1\Delta\hat{t}/2), \tag{38}$$

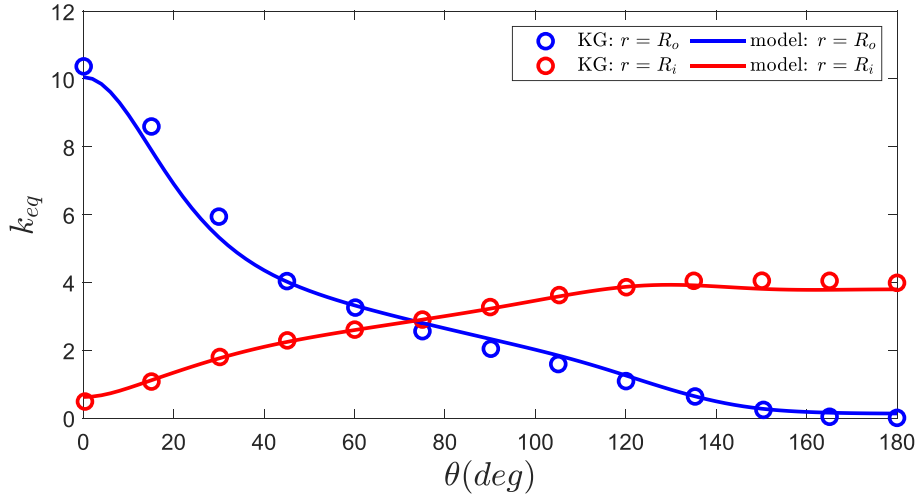$$\mathbf{k}_3 = \mathbf{f}(\hat{t}_n + \Delta\hat{t}/2, \mathbf{q}^n + \mathbf{k}_2\Delta\hat{t}/2), \tag{39}$$

$$\mathbf{k}_4 = \mathbf{f}(\hat{t}_n + \Delta\hat{t}, \mathbf{q}^n + \mathbf{k}_3\Delta\hat{t}). \tag{40}$$

3.3. Global stability analysis

Once the steady-state solutions are obtained, $[\hat{\Psi}_s, \hat{\Phi}_s]^T$, we can perform a global stability analysis of the solution just defining a small variation of the solution around the steady-state solution,

$$\mathbf{q} = \mathbf{q}_s + \mathbf{q}'. \tag{41}$$

Fig. 3. Comparison between the experimental local equivalent conductivity $\bar{k}_{eq}$ by Kuehn and Goldstein (KG) [6] with the current numerical results (model) at $Ra = 4.7 \cdot 10^4$ and $Pr = 0.706$.

If we define the perturbations $\mathbf{q}' = [\hat{\Psi}', \hat{\Phi}']^T$ to be of the form,

$$\mathbf{q}'(\hat{r}, \theta, \hat{t}) = \tilde{\mathbf{q}}(\hat{r}, \theta)e^{\lambda \hat{t}}, \tag{42}$$

the stability equations reduce to solving a generalized eigenvalue problem of the form,

$$\mathbf{B}\tilde{\mathbf{q}} = \lambda \mathbf{A}\tilde{\mathbf{q}}, \tag{43}$$

with $\mathbf{A}$ and $\mathbf{B}$ differential operators defined previously and $\lambda = \lambda_r + i\lambda_i$ and $\tilde{\mathbf{q}}$ denoting the complex eigenvalue and eigenvector, respectively.

Unlike in the steady solver, symmetry has not been forced in the stability analysis. It means that steady solution $\mathbf{q}_s$ has been previously unfolded so that the stability analysis is applied over the full angular domain $\theta \in [0, 2\pi]$.

3.4. Validation

For validation purposes the developed model has been solved using a mesh of $N_r \times N_\theta = 30 \times 91$ nodes (where 91 nodes span half of the angular domain). Its numerical solutions have been compared with the experimental results presented by Kuehn and Goldstein [6]. In Fig. 3 we can see the value of k_{eq} at the inner and outer surfaces for $Ra = 4.7 \cdot 10^4$ and $Pr = 0.706$ obtained from the simulations made by the spectral code for different angular values (θ), compared to the results obtained experimentally. It is noted that the numerical predictions are consistent with the experimental results measured on the surfaces of the concentric cylinders in [6].

Fig. 4 shows the results of the dimensionless temperature field as a function of the dimensionless radial coordinate inside the fluid, for different values of θ compared to the experimental results obtained for the same case in [6]. It presents an excellent agreement. Finally, Table 1 summarizes the results of $\bar{k}_{eq}$ measured varying the values of Ra and Pr for $A = 1.25$, and as it can be seen, values are obtained that vary in the third decimal place when they are compared to those of [24]. It is worth noting that due to conservation of energy any steady-state solution should verify that $\bar{k}_{eq,o} = \bar{k}_{eq,i}$ and this is observed for our numerical results up to the fifth decimal place.

4. Numerical results

This section details the procedure to obtain the complete map of steady-state solutions and shows the regions in the parameter

Table 1

Comparison of the average equivalent conductivity $\bar{k}_{eq}$ obtained by the current model with the experimental results provided by Kuehn & Goldstein [6] where inner and outer values are displayed separately. Current results are likewise compared with other numerical solutions provided in literature [24].

			$\bar{k}_{eq}$			
Ra	Pr	$A \equiv D_i/L$	$\bar{k}_{eq,i}$ [6]	$\bar{k}_{eq,o}$ [6]	$\bar{k}_{eq,io}$ [24]	$\bar{k}_{eq,io}$ (current)
10^2	0.7	1.25	1.000	1.002	1.001	1.001
10^3	0.7	1.25	1.081	1.084	1.082	1.082
$3 \cdot 10^3$	0.7	1.25	1.404	1.402	1.397	1.397
$6 \cdot 10^3$	0.7	1.25	1.736	1.735	1.715	1.715
10^4	0.7	1.25	2.010	2.005	1.979	1.978
$2 \cdot 10^4$	0.7	1.25	2.405	2.394		2.374
$3 \cdot 10^4$	0.7	1.25	2.661	2.643		2.624
$5 \cdot 10^4$	0.7	1.25	3.024	2.973	2.958	2.958
$7 \cdot 10^4$	0.7	1.25	3.308	3.226		3.193
10^4	0.5	1.25	1.950	1.955		1.924
10^4	1.0	1.25	2.038	2.039		2.009
10^4	5.0	1.25	2.069	2.066		2.039
$3 \cdot 10^4$	5.0	1.25	2.741	2.768		2.655
$5 \cdot 10^4$	5.0	1.25	3.036	3.088		2.976
10^5	5.0	1.25	3.756	3.471		3.486
10^4	10.0	1.25	2.070	2.067		2.040
10^4	100.0	1.25	2.071	2.067		2.041

space where they are stable, which have been verified by a global stability study, as well as by solving the temporal evolution of the equations (28)–(30). All the results presented in this research correspond to $A \equiv D_i/L = 1.25$.

4.1. Map of steady state solutions

The first problem to be addressed is the determination of steady-state solutions in a $Pr - Ra$ map. This is shown in Fig. 5. To obtain this map, we have visited the different position of $Ra \in [10^2, 5 \cdot 10^6]$ and $Pr \in [0.01, 1]$ dividing the map in 75 and 149 points respectively according to a logarithmic scale. Therefore, this study aims to provide the steady state solution for 11175 cases in the range of Ra and Pr used. Firstly, Pr number is fixed and we increase the Ra number, solving the steady-state solution by means of Newton-Raphson iteration using as initial guess the result obtained for the previous Ra. After that sweep of the map, we repeat the process fixing Ra and increasing/decreasing Pr numbers from $10^{-2}/1$, respectively. This new sweep allows to obtain regions of dual steady-state solutions [40]. In Fig. 5 the different solutions are
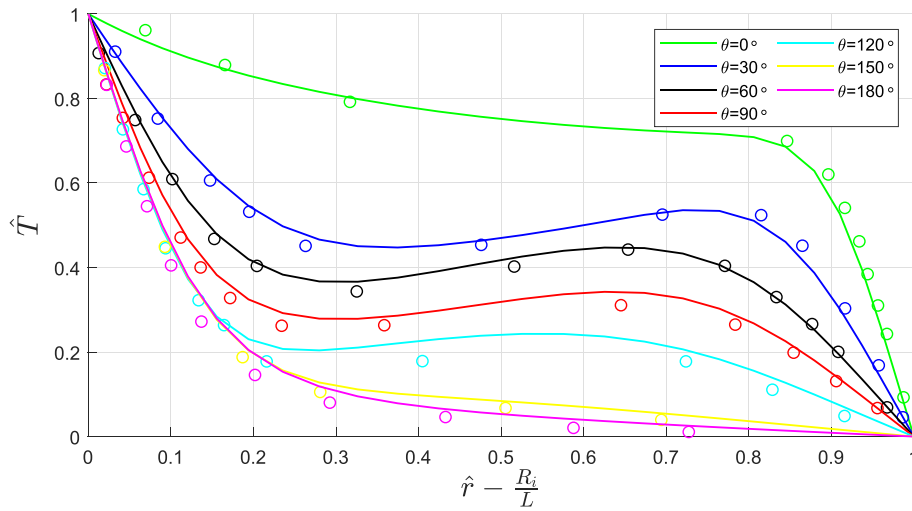
Fig. 4. Comparison between the experimental dimensionless radial temperature (circles) by Kuehn and Goldstein [6] with the current numerical model (continuous line) at $Ra = 4.7 \cdot 10^4$ and $Pr = 0.706$.
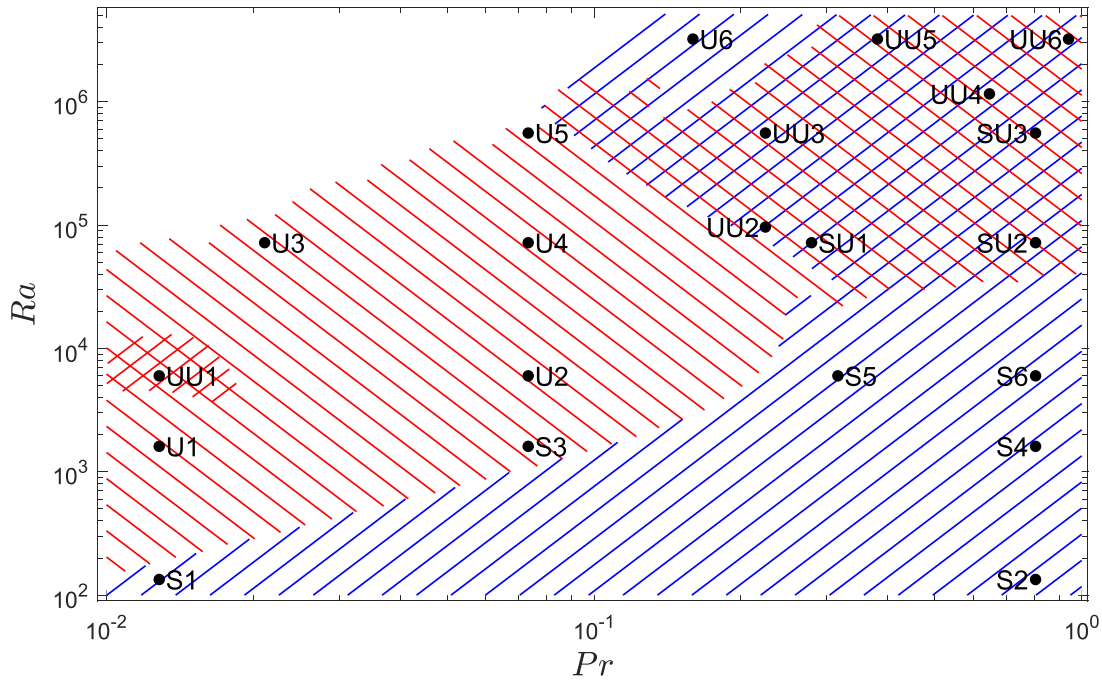

Fig. 5. Map of steady solutions for $A = 1.25$ in the (Pr, Ra) space. Some of the solutions analysed later are marked with name S for stable solutions and U for unstable solutions.

marked, together with the special cases presented later. The solutions in the region hatched with lines sloping up to the right (blue lines) present a steady solution with one vertical plume emanating from the upper part of the inner cylinder. In the region hatched with lines sloping up to the left (red lines) the problem presents multiple plumes. The solutions used to discuss the structures created are marked by points and named using letters, S means that the solution is stable and U if unstable. There are regions where two steady-state solution coexist marked by two different letters, UU or SU depending whether both solutions are unstable or one stable and another unstable. Results of stability are discussed later. This map complements and fill the gaps of the work of [36], where they presented only 24 different points in the $Ra - Pr$ domain (see Fig. 10).

Fig. 6 shows the stream function isocontours and isotherms of all the steady-state solutions where only a single solution has been

found (single hatch pattern). The solutions for low Ra present a structure of two counter-rotating symmetrical vortices with respect to the y axis. For a given low Ra number ($Ra = 1.3397 \cdot 10^2$), increasing the Prandtl number we find the transition from solution S1 to S2, which basically increases the intensity of the rotation of the vortices and move their centers upwards. For $Pr = 0.8043$, increasing the Ra number, the solutions present the same kind of structure, but the intensity of the vortices increase and the center climbs up over the vertical height of the center of the annulus (see solutions S4 and S6). It can be also observed the appearance of an intense vertical plume where the temperature is maximum, placed on the y axis. For intermediate Pr numbers ($Pr = 0.0733$, the solution passes from a stable solution in which the typical two counter-rotating vortices are deformed into four counter-rotating ones, to a solution where the flow is dominated by 6 counter rotating vortices (see transition from S3 to U2, U4). If the Rayleigh
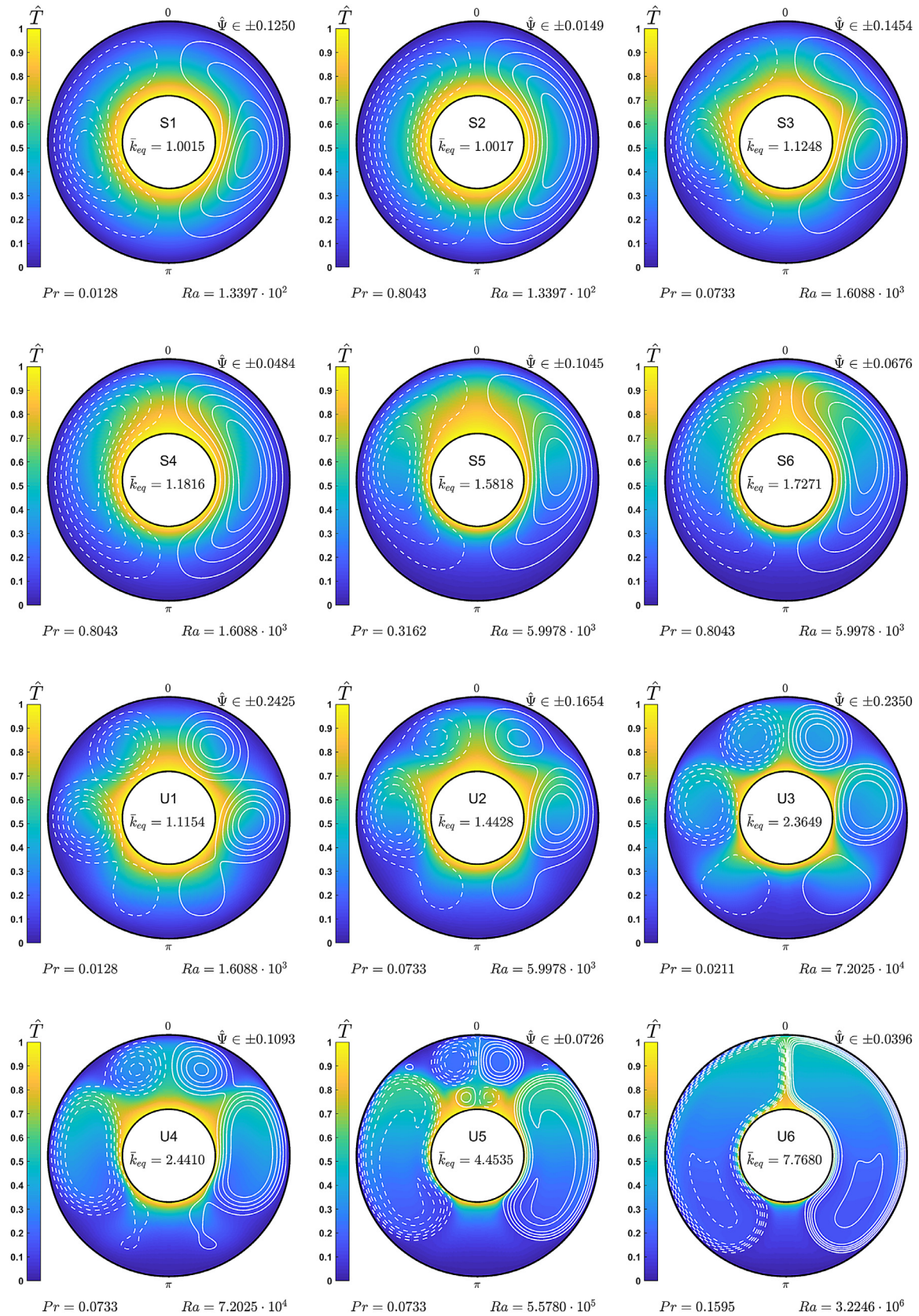
Fig. 6. Steady solutions corresponding to the region of the map (Fig. 5) where only single steady solutions have been found. S and U stand for stable and unstable steady solutions respectively. Dimensionless temperature $\hat{T}$ have been plotted through colormap whereas isocontours describe the dimensionless stream function $\hat{\Psi}$.

number is further increased, the vortices at the upper part scale up in intensity and dominate (U5), creating a vertical plume that complicates further the structure of the flow in that region. It is worth noting that the temperature field near the inner surface shows an evolution from 5 plumes (U1, U2, U3) to 2 (U4 and U5). Finally, when Ra number is dominant (solution U6, for $Ra = 3.2246 \cdot 10^6$ and $Pr = 0.1595$, the solution becomes a very intense plume flowing from the upper part of the inner cylinder. This kind of solution can be referred to as upwards vertical plume, since at the vertical axis (y axis) the plume flows in the vertical direction.

Regarding the two regions of dual steady-state solutions (regions with double hatch pattern), we show in Fig. 7 the two steady-state solutions found for the cases UU1, UU2 y UU3. The first case, UU1 corresponds to the region of dual solution for low values of Pr ($Pr = 0.0128$). Both solutions present basically the same structure with five plumes. Solutions UU2 to UU6 present two steady-state solutions, one with a very intense upward vertical plume, and the other one with 3 plumes, one vertical and the other one placed at $\theta_{crit} \approx 31.5°$. As we will discuss later, the solution with the upward vertical plume is the real attractor for the unsteady solution.

Fig. 8 shows the flow structure in the dual solution region SU. There is a steady solution, that is the solution with one upwards vertical plume, and there also are another unstable solution presenting two plumes at angles $\approx 31.5°$ as before.

As we have shown in this section, the structure of the steady solutions obtained can be of a simple vertical plume or multiples plumes. The case of a single plume is easy to understand comparing with the results shown in [21] for an axisymmetric case, [41] for a 2D case of a variable density jet and [42] for a confined 2D jet/wake. Buoyancy forces are so intense that, due to the geometry of the problem, the boundary layer on the upper side of the inner cylinder starts to heat up the fluid creating a single planar jet. The force that generates the 2D jet is the buoyancy force that tries to initiate the movement of the fluid upwards, and once the movement has started, the flow becomes a planar variable density jet similarly to the one described in [41]. For Prandtl numbers of the order of unity, thermal and viscous diffusion becomes of the same order, and the described flow is created. However, for low Pr numbers, the viscous diffusion is much lower than the thermal diffusion, allowing the appearance of more complicated structures. In these cases, two plumes are created at approximate angles of $31.5°$ on both sides of the symmetry plane. This allows to create a descending flow at the mid plane that moves against the buoyancy forces. The structure created can be described as two very interrelated counter-rotating vortices near the midplane. The stability characteristics of these more easily destabilized situations are analyzed in the next section.

4.2. Global stability

Once the map of steady-state solutions to the problem of natural convection between two concentric cylinders has been obtained and described, it would be interesting to carry out a global stability analysis in order to elucidate the stability properties of each of the steady solutions found. To perform this task, the global stability equations described in Section 2 are used. Fig. 9(a) shows the most unstable mode for the case of $Pr = 0.0733$ as a function of the Rayleigh number. It is detected that the change of sign of the exponent λ occurs approximately for the critical value $Ra_{crit} \approx 2438$. The eigenvector structure (real part) of the most unstable mode is also represented in Fig. 9(b), (c) and (d) for the cases labelled S3, U2 and U4, respectively in the stability map. It can be seen that the structure is that of a sustained oscillation around the two $31.5°$ plumes. It is worth mentioning that while S3 and U2 solutions os-

cillate with a given frequency $\lambda_{max,i} \neq 0$, the last solution U4 only has a non-null (positive) real part in the eigenvalue.

Finally, repeating the process for all the Pr number studied we have obtained the global stability map for the flow in this problem configuration ($A = 1.25$). This is shown in Fig. 10. The stability border (black continuous line) delimits the region of the $Pr - Ra$ map in which there is at least one stable steady solutions. As we will see below, this stable solution turns out to be the physical solution of the steady problem. It is worth mentioning that below the stability curve, the stable solutions are defined by a unique upwards vertical plume (hatch pattern with lines sloping up in blue color), but for low values of Pr ($Pr \leq 0.2$ approximately) there is a small region of steady stable solutions with multiple plumes (hatch pattern with lines sloping down in red color). This numerical stability curve has been tested by means of unsteady numerical simulations in different points, obtaining the same values of Ra_{crit} for the transition, where the whole angular domain $\theta \in [0, 2\pi]$ has been regarded (no symmetry imposed). As it will be shown in the following section by means of transient simulations, whenever there is a solution with a vertical plume structure, it will act as a flow attractor. Therefore, the stability in the area of $Pr \gtrsim 0.25$ is dominated by the stability of that solution and that is what is finally represented in Fig. 10. Fig. 10 also displays some cases of the stability test by Yang *et al.* [36] accomplished by means of transient analysis. According to them, four states are regarded (see legend of Fig. 10): UP1 (unstable with one plume), UPM (unstable with multiple plumes), SP1 (stable with on plume) and SPM (stable with multiple plumes). It can be observed that the region with stable solutions resembles with the stable region found in the current research work. The only significant discrepancy is based on the observations made in the case where $Pr = 0.1$ and $Ra = 10^5$. Unlike the conclusion drawn by the aforementioned authors, as far as we have found, it seems to behave as an unstable solution, where the physical solution is a sustained oscillation around the steady state solution.

As we discussed previously, the typical flow structures may contain a simple or multiple plumes. In the case of the simple plume, the buoyancy force creates the planar variable density jet. Bharawaj and Das [41] discussed that the only global instability that appear in this flow is a 'puffing' plume (varicose instability) but the one presented here is of sinuous type (see supplementary material). This instability is created due to the competition between the inertia and viscous forces in the shear layers of the planar jet. The flow can be seen as an oscillation over the steady state solution (equilibrium solution) as it can be observed in Fig. 10 by Tammisola et al. [42]. The case of multiple plumes have a more complex equilibrium. The structure that appears on the upper part of the cylinder is formed by two ascending plumes placed at approximately $31.5°$ on both sides of the symmetry plane and a descending flow at the mid plane creating two counter-rotating vortices. As we have discussed previously, these cases are mainly controlled by thermal diffusion, so when they are in equilibrium, the heat transfer created on both cylinders and the convection due to the counter-rotating vortices equilibrate. If Ra is increased over a threshold, this heat transfer equilibrium is lost so the entire flow is destabilized, moving the solution to a single-point attractor as it is explained in the following subsection. The cause of the instability is created outside of the ascending jets, as it can be observed in figures 9(b)-(c) where the structure of the most unstable mode for the same low Prandtl number ($Pr = 0.0733$) and three different Rayleigh numbers are plotted. The eigenvector corresponding to the most unstable mode has their maxima at approximate angles of $45°$ in the lower region of the ascending jets so those parts will be the first destabilized to a new solution instead of oscillating around the steady state.
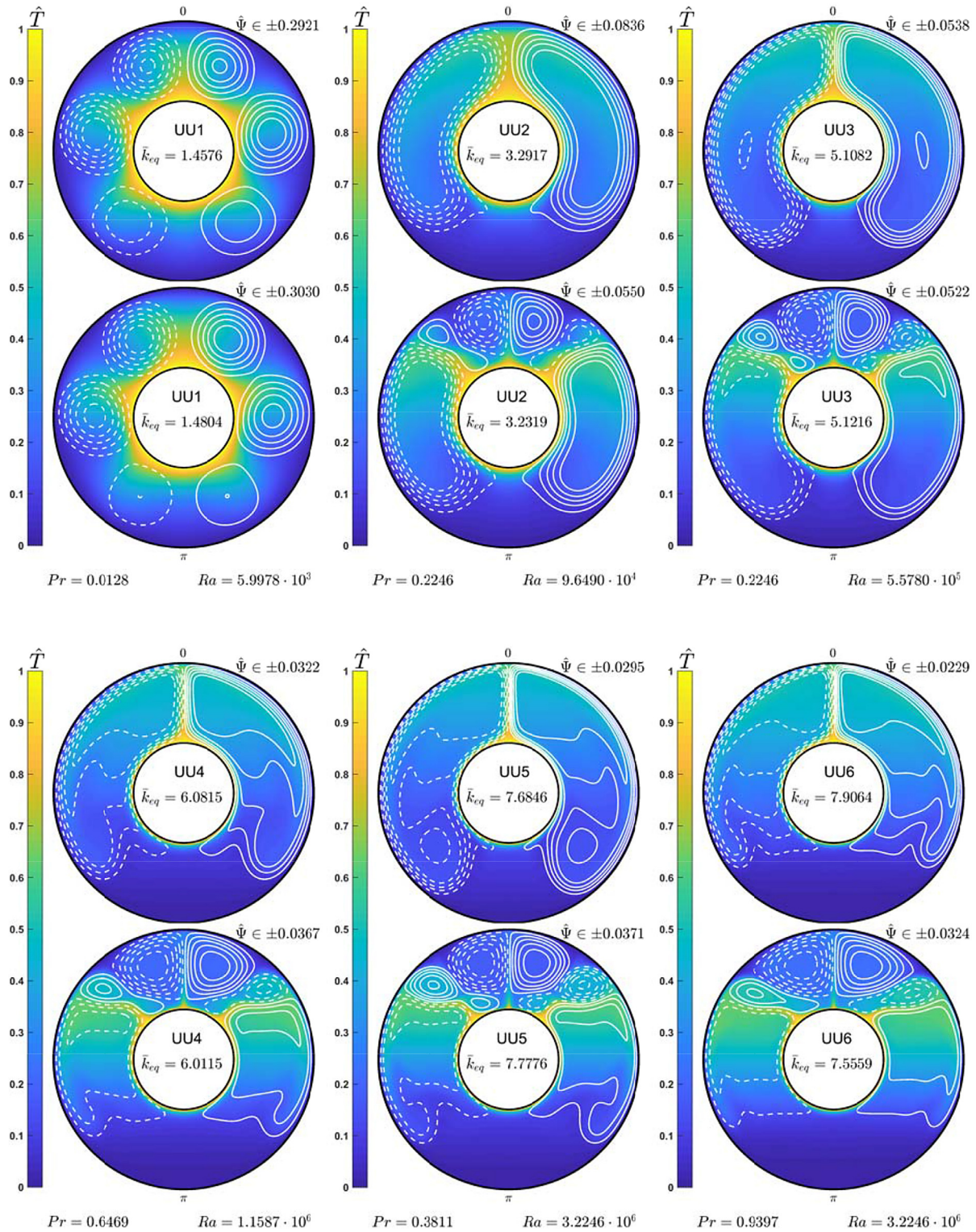
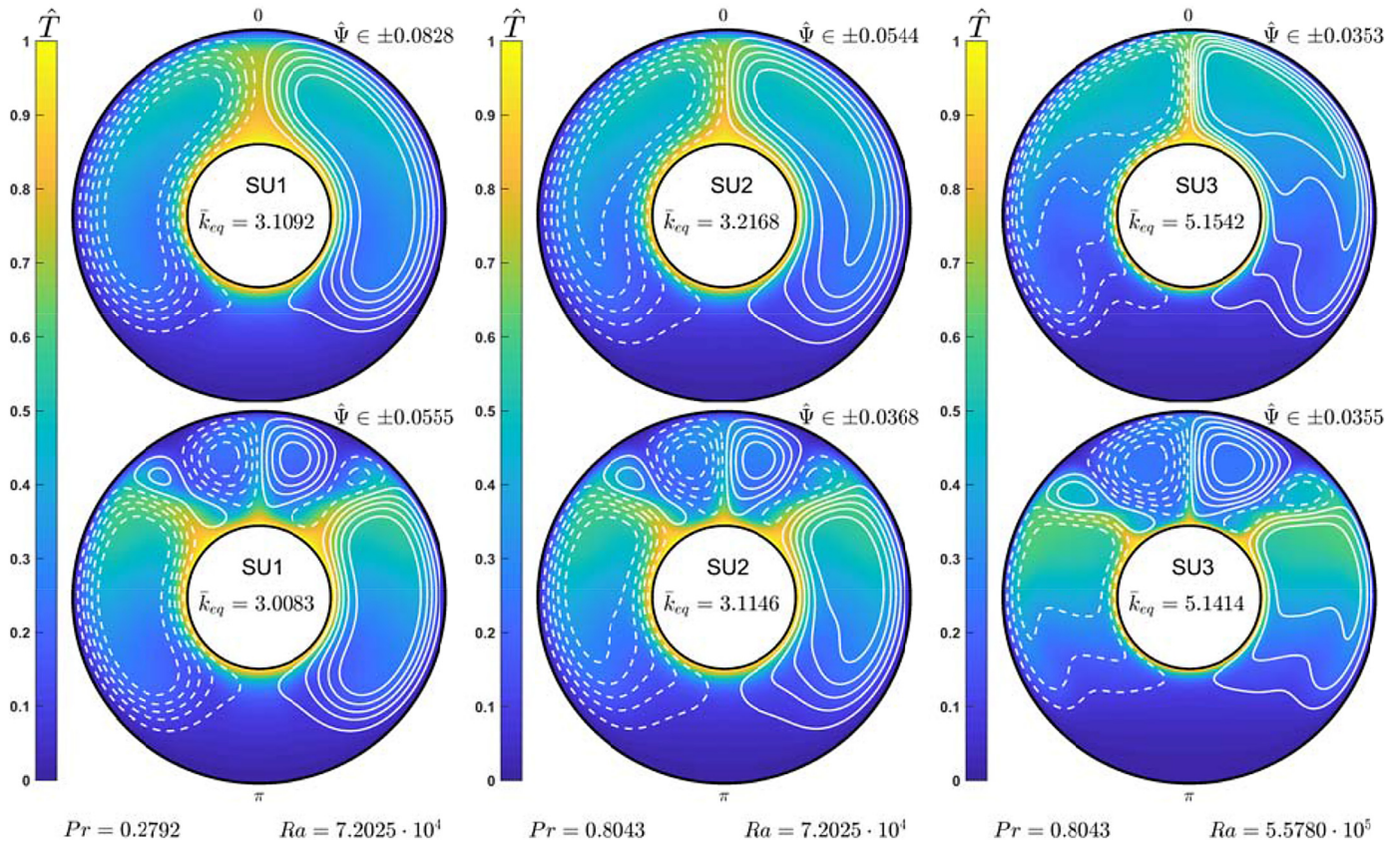**Fig. 7.** Steady solutions corresponding to the region of the map (Fig. 5) where two unstable steady solutions coexist (UU). Dimensionless temperature $\hat{T}$ have been plotted through colormap whereas isocontours describe the dimensionless stream function $\hat{\Psi}$.

4.3. Unsteady solutions in the unstable region

Having accurately determined the region of stability of steady-state solutions it would be interesting to understand what is physically happening in the unstable region. To this end, unsteady numerical simulations have been carried out in different regions.

Firstly, two specific cases of temporal evolution of the flow for points included in dual solution regions will be studied. Fig. 11 shows the results for $Pr = 0.2792$ and $Ra = 7.2025 \cdot 10^4$, corresponding to the dual SU1 solution. Each temporal evolution takes as initial solution the steady state solution of the two possible ones that coexist in that region and, to accelerate the process, white

Fig. 8. Steady solutions corresponding to the region of the map (Fig. 5) where two steady (stable and unstable solutions) coexist (SU). Dimensionless temperature $\hat{T}$ have been plotted through colormap whereas isocontours describe the dimensionless stream function $\hat{\Psi}$.
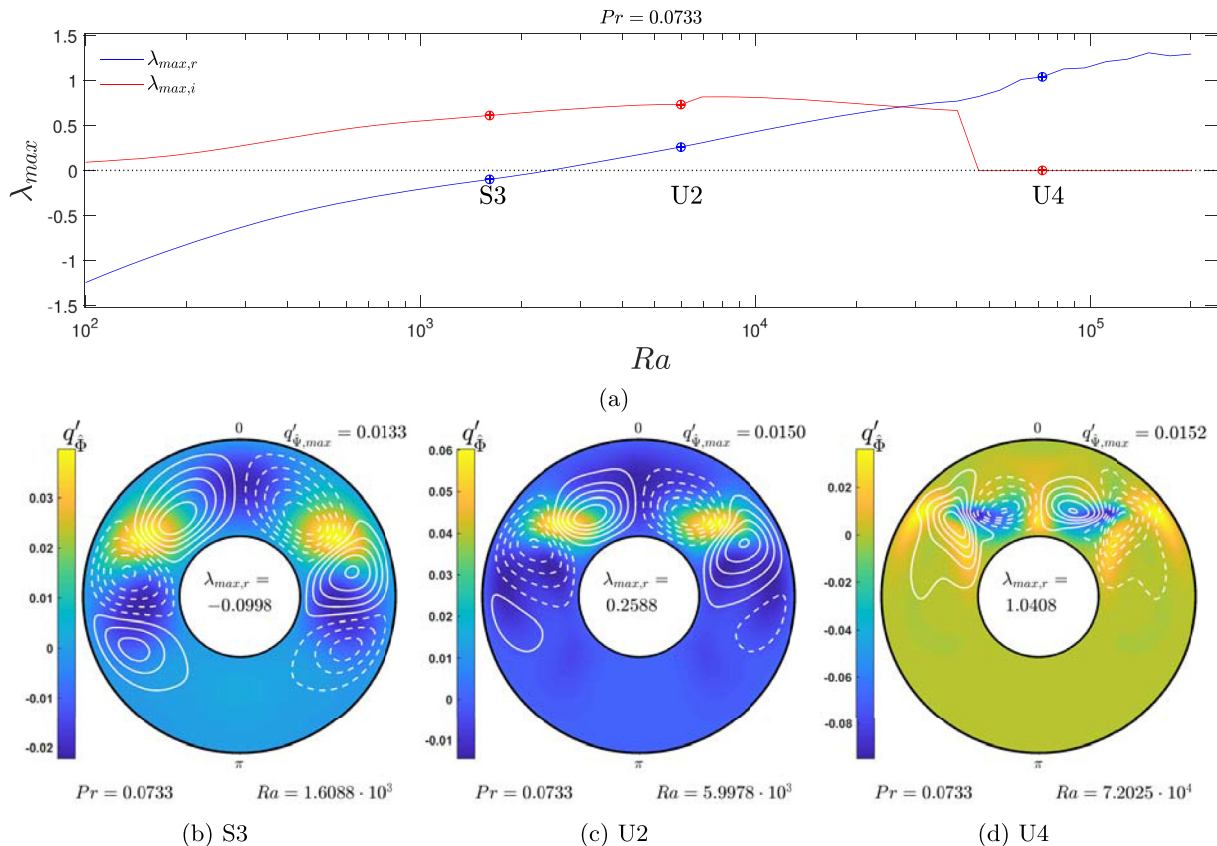
Fig. 9. Evolution of the real and imaginary parts of the most unstable mode (mode with the biggest real part λ_{max}) (a) for $Pr = 0.0733$. Real part of the eigenvector of the most unstable mode for steady solutions $S3$(b), $U2$(c) and $U4$(d).
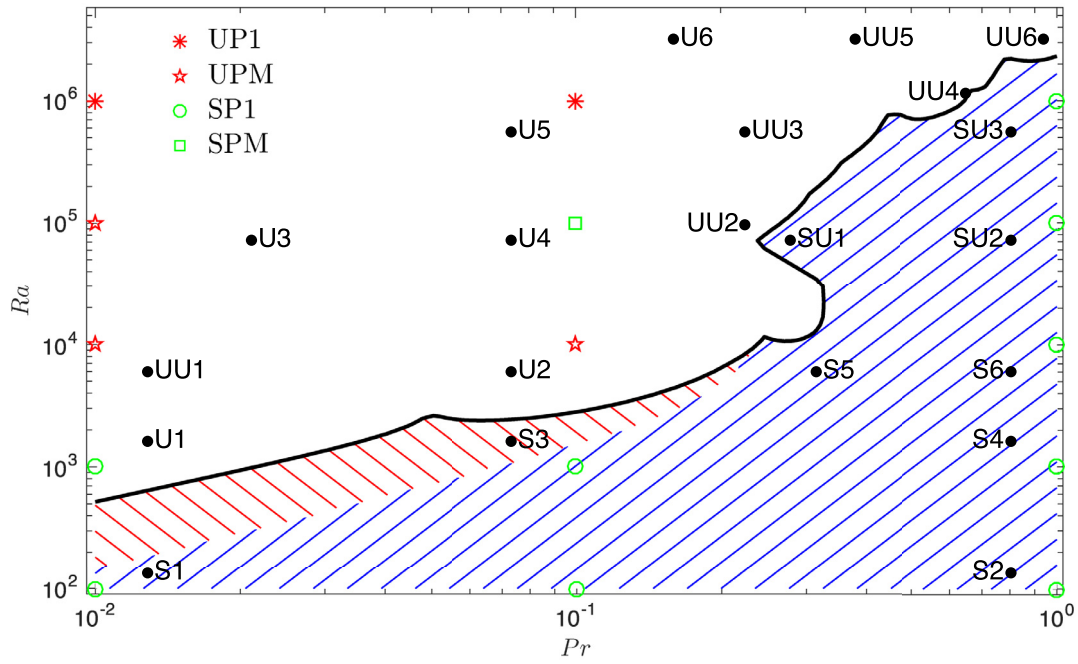
Fig. 10. Stability map for $A = 1.25$. The stable and unstable regions are separated by the marginal black curve $Ra_m = f(Pr)$. The diagram provided in [36] is also shown using green and red symbols for the stable and unstable solutions, respectively. (For interpretation of the references to color in this figure legend, the reader is referred to the web version of this article.)

noise of intensity 10^{-4} is added to the stream-function with the following form:

$$\Psi = \Psi_s + \sin\left[\pi\left(\hat{r} - \frac{A}{2}\right)\right]\cos\left(\theta - \frac{\pi}{2}\right) \cdot 10^{-4}. \tag{44}$$

The solution in blue in Fig. 11(g), being stable, remains on the same value of $\bar{k}_{eq}$ throughout the entire process as shown in Fig. 11(a). The solution in red comes from the unstable solution. Initially it causes some oscillations (b) until the corresponding quasi-steady-state solution with $\bar{k}_{eq} \approx 3.38$ dominates (c), whose shape has a double plume structure in angles $\pm 31.5°$ with respect to the y axis. After about 1200 (dimensionless) units of time, the solution becomes unstable and quickly switches to the stable solution (d)-(f). In Fig. 11(h) it is presented the Poincaré map of the time evolution of the solutions presented using as measurement parameters $\bar{k}_{eq,i}$ and $\bar{k}_{eq,o}$. As it has been mentioned earlier, any steady state solution has to verify that $\bar{k}_{eq,i} = \bar{k}_{eq,o}$, so we have included in the plot that line to show that the solutions have to lie around it. The first case starts from the final steady solution and it rests there because the solution is stable. For the unstable case, it starts from a steady solution, jumps to an intermediate solution (Fig. 11(c)) that has a greater value of $\bar{k}_{eq}$ and that is quasi-steady (lie over the red line), to later return to the steady state solution characterized by one upwards vertical plume, that acts as an attractor of the solution in this particular case. The quasi-stationary intermediate solution has an equivalent average conductivity of $\bar{k}_{eq} \approx 3.38$ that is around 10% higher than the final steady solution. The intermediate solution consists of a downward vertical plume, since the flow goes following the downright direction along the y axis. The above explanation is supported by a video, included as supplementary material, which displays the transient evolution of the dual solution (SU1).

Secondly, the time evolution of the UU2 solution shown in Fig. 12 will be analyzed. The same technique described in the previous paragraph will be used, in which the problem is initialized from each of the steady-state solutions present for $Pr = 0.2246$ and

$Ra = 9.6490 \cdot 10^4$ by adding the same small perturbation to the stream function solution defined in Eq. (44). The solution with only one vertical plume (Fig. 12(a)–(d) and blue line in Fig. 12(j)) leaves the steady-state solution shown in Fig. 12(a), and after approximately 400 (dimensionless) time units, the flow is destabilized and starts oscillating and forming a flickering instability in the plume (see the video upload as supplementary material) whose structure is shown in Fig. 12(c)-(d). Similarly, if transient simulation is initiated from the second steady solution displayed in Fig. 12(e) it evolves until it finds again a quasi-steady-state solution with two plumes ($\bar{k}_{eq} \approx 3.6$), detailed in Fig. 12(f). It remains there for approximately 800 characteristic times, jumping to the attractor solution, which in this area is characterized by an intense high frequency oscillating plume (Fig. 12(h)-(i)). We plot again the Poincaré map for both solutions in Fig. 12(k) and (l). Both solutions start from the steady-state solution calculated by means of Newton-Raphson and move to the same attractor that corresponds to a vertical oscillating plume. Note that Fig. 12(c)-(d) and (h)-(i) display the same oscillating vertical plume, where the oscillation amplitude and its center is the same in both cases. It is relevant to point out that the solution with multiple plumes (Fig. 12(e)-(i)) passes through a quasi-steady solution (Fig. 12(f) with $\bar{k}_{eq} \approx 3.57$) which enhances by 10% the heat transfer process.

Finally, it remains to answer the question of what is happening throughout the unstable zone. As we have seen, in dual-solution regions, whenever a single plume solution could exist, it will always provide the lower energy dissipation and would work as a basin attractor. We have checked the cases shown in Fig. 5 and for them, whenever the solution is in the region hatched with lines sloping up to the left (blue color), the final solution is always a vertical plume placed in the upper part of the inner cylinder. Whenever the solution is in the stable region shown in Fig. 10, the vertical plume is stable, and in the unstable region the solution presents a flickering instability. In the unstable region hatched with lines sloping up to the left (red color) in Fig. 5, the solution presents multiple plumes. The final non-stationary solution is always a solution that resembles the single vertical plume or multi-
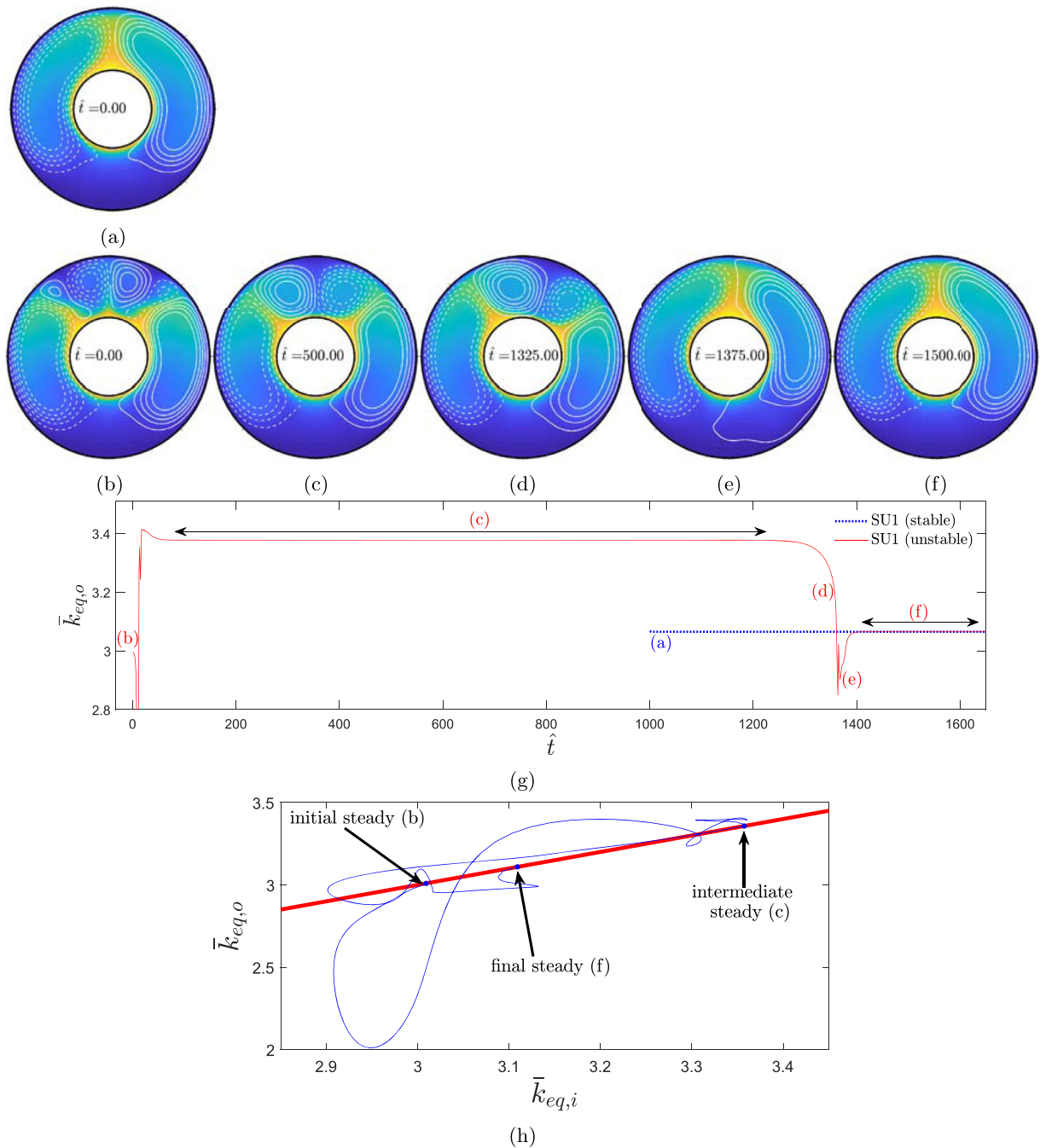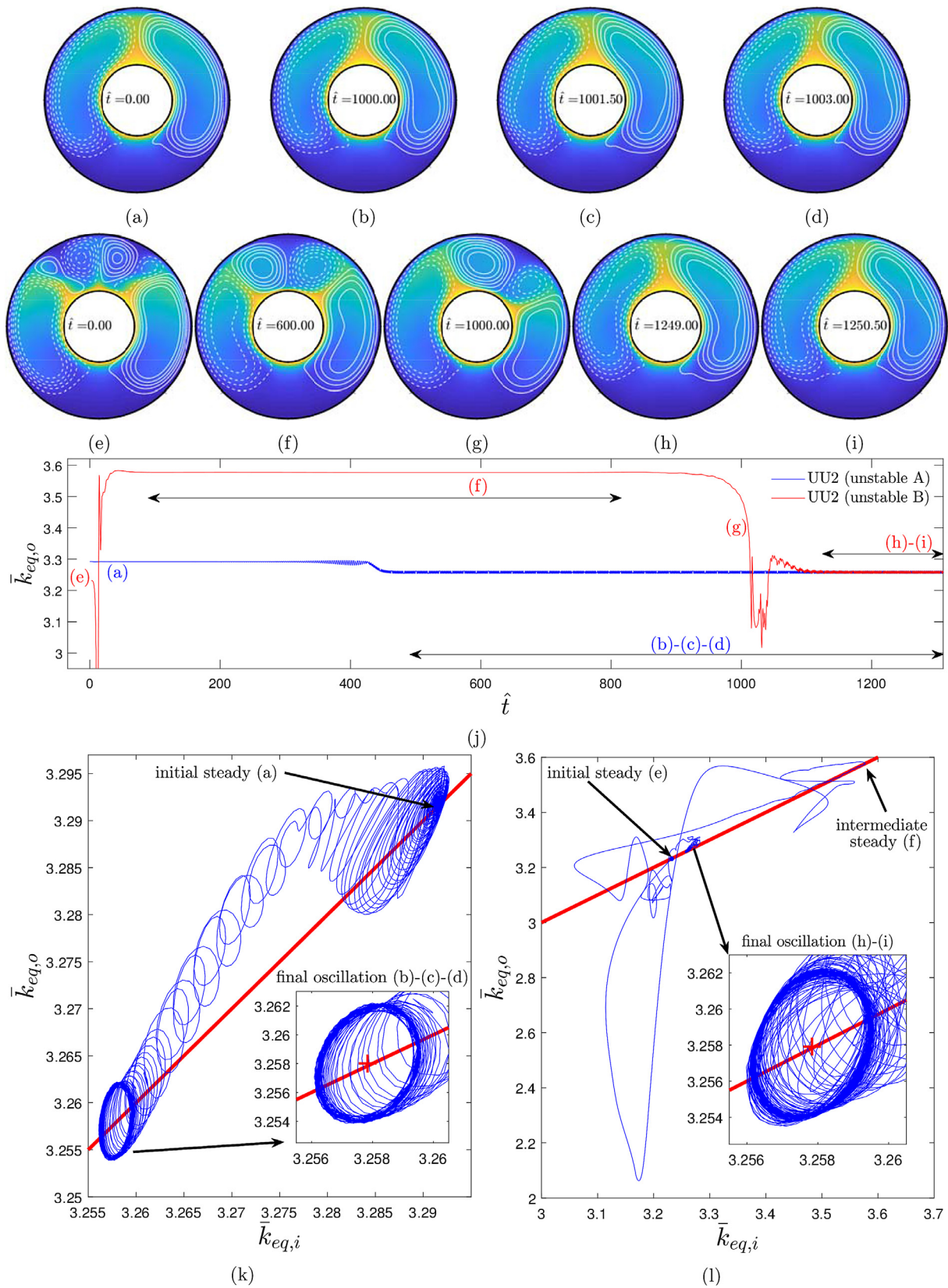
Fig. 11. Transient evolution starting from the dual steady solution SU1 ($Pr = 0.2792$ and $Ra = 7.2025 \cdot 10^4$). As it can be seen in subfigure (a), transient simulation starting from the SU1 stable state remains stable in the form of an upward plume. However, if transient simulation is launched from the SU1 unstable steady solution (displayed in subfigure (b)) it evolves to an intermediate quasi-steady solution (subfigure (c) at $\hat{t} = 500$) which through an asymmetric transition evolves to the final steady state (subfigure (f) at $\hat{t} = 1500$) which is the same solution as the initial stable case displayed in subfigure (a). Subfigure (g) shows the time evolution of the average equivalent conductivity in both transient simulations. As expected, both simulations reach the same final solution (subfigures (a) and (f)). Subfigure (h) shows the Poincaré map of the SU1 unstable time evolution where the red line is the region where $\bar{k}_{eq,i} = \bar{k}_{eq,o}$. Blue line displays the path followed by the flow displayed in subfigures (b)–(f). As expected, all steady solutions are on the red line. (For interpretation of the references to color in this figure legend, the reader is referred to the web version of this article.)

ple plume solutions, depending on the (Pr, Ra) values used. From the physical point of view, one may think that solutions that minimize heat transfer between surfaces are the ones that will be candidates to be the attractors of the system, but in the two examples above it is observed that this is not always the case. In the cases displayed in Figs. 11(g) and 12(j) it can be seen that of the dual solutions analyzed, the solution of multiple plumes always presents a $\bar{k}_{eq}$ lower than the final solution determined by the single plume attractor. For this reason, $\bar{k}_{eq}$ is not a parameter that directly con-

ditions the solution that nature selects, and a much more detailed study of all the possible non-stationary solutions that this problem presents should be performed. Furthermore, the fact that we have found almost stationary solutions to the problem that improve heat transfer mechanism in this type of problem (remember that in this systematic study a constant value of $L/D_i = 0.8$ has been maintained) allows us to suspect that geometric modifications can be made to the shape of the inner surface that will stabilize these solutions. This strategy, in case it was successful,

Fig. 12. Transient evolution starting from the dual steady solution UU2 ($Pr = 0.2246$ and $Ra = 9.6490 \cdot 10^4$). As it can be seen in subfigures (a)–(d) transient simulation starting from the first unstable steady solution (subfigure (a)) evolves towards a final sustained oscillation (subfigures (b)–(d)). Subfigures (e)–(i) represent the time evolution of the flow starting from the second unstable steady (displayed in subfigure (e)). Like in the first case, the second steady solution also evolves towards the same sustained oscillation but after passing through an additional intermediate quasi-steady state plotted in subfigure (f) at $\bar{t} = 600$. This fact can be checked in subfigure (j). Subfigures (k) and (l) display the Poincaré maps for each simulation. It can be observed that final oscillations have the same amplitude and evolve around the same point located at $\bar{k}_{eq} \approx 3.258$.

can be used to improve the heat transfer process in real applications.

5. Conclusions

In this study, a systematic characterization of the steady-state solutions of the flow between two concentric cylinders heated at different temperatures, with a constant $L/D_i = 0.8$ for a parameter space $Pr \in [0.01, 1]$ and $Ra \in [1000, 5 \cdot 10^6]$ has been carried out. More than 11000 steady-state solutions have been sought, being, as far as the authors know, the most detailed study so far for this type of configurations. Generally, solutions for $Pr > 0.25$ have a vertical plume anchored to the top of the inner cylinder. However, when $Pr < 0.25$, if Ra is low enough it shows a single plume which evolve to solutions with multiple plumes as Ra increases. An overall stability analysis has been performed on all the steady-state solutions, and the value of the threshold Ra_{crit} for each Pr, for which the solution becomes unstable, can be determined quite precisely. This supercritical transition presents a complex curve due to the complicated $2D$ structure of the steady-state solutions with respect to planar Rayleigh-Bénard problem.

The stability diagram has been checked by means of time evolution simulations in different cases reproducing accurately the transition. For some of the total cases studied, the temporal evolution shows that in the region in which one expects a simple intense buoyancy plume, this solution acts as an attractor, showing that it is the dominant solution to be expected in nature (steady of unsteady). The region of multiple plumes is wider typically for $Pr < 0.25$. For low Ra numbers one expect to have one vertical steady plume. There is a limit when those steady solutions become solutions with multiples plumes (2,3 or 6 plumes depending on the values of $Pr - Ra$). The lower the Pr the more plumes appear in the solution. In addition, if a single-plume solution exists, it will always be the attractor of the system in both the unstable and stable region. However, if this solution does not exist, in the unstable region we will find oscillating solutions with multiple plumes.

Finally, the temporal evolution code developed here to observe the behaviour of the dual solution regions has been used and the existence of quasi-steady intermediate solutions has been discovered. They present heat transfer values almost 10% more intense than the final attractor for the same values of (Pr, Ra), being good candidates for a future realization of some type of passive control to improve heat transfer in this type of devices. As additional future work, it is expected to study the effects of the aspect ratio (A) on the stability map and, more specifically, to give new insights about how it affects the evolution of the marginal curve Ra_m.

Declaration of Competing Interest

The authors declare that they have no known competing financial interests or personal relationships that could have appeared to influence the work reported in this paper.

CRediT authorship contribution statement

J.J. Serrano-Aguilera: Conceptualization, Methodology, Software, Validation, Formal analysis, Investigation, Data curation, Writing - original draft, Visualization, Funding acquisition. **Francisco J. Blanco-Rodríguez:** Conceptualization, Methodology, Formal analysis, Investigation, Data curation, Writing - original draft, Writing - review & editing, Visualization, Funding acquisition,. **L. Parras:** Conceptualization, Formal analysis, Investigation, Writing - original draft, Writing - review & editing, Funding acquisition.

Supplementary material

Supplementary material associated with this article, which consist of two videos showing transient evolution of SU1 (Fig. 11) and UU2 (Fig. 12) cases, can be found, in the online version of the manuscript, at doi:10.1016/j.ijheatmasstransfer.2021.121151

References

[1] F.H. Busse, Non-linear properties of thermal convection, Rep. Prog. Phys. 41 (12) (1978) 1929–1967, doi:10.1088/0034-4885/41/12/003.

[2] A. V. Getling, Advances Series in Nonlinear Dynamics, vol. 11, pp. 1–8. 10.1142/9789812796356_0001.

[3] A. Fernández-García, E. Zarza, L. Valenzuela, M. Pérez, Parabolic-trough solar collectors and their applications, Renew. Sustain. Energy Rev. 14 (7) (2010) 1695–1721, doi:10.1016/j.rser.2010.03.012.

[4] X.-D. Shang, X.-L. Qiu, P. Tong, K.-Q. Xia, Measured local heat transport in turbulent Rayleigh-Bénard convection, Phys. Rev. Lett. 90 (2003) 074501, doi:10.1103/PhysRevLett.90.074501.

[5] X. He, D. Funfschilling, H. Nobach, E. Bodenschatz, G. Ahlers, Transition to the ultimate state of turbulent Rayleigh-Bénard convection, Phys. Rev. Lett. 108 (2012) 024502, doi:10.1103/PhysRevLett.108.024502.

[6] T.H. Kuehn, R.J. Goldstein, An experimental and theoretical study of natural convection in the annulus between horizontal concentric cylinders, J. Fluid Mech. 74 (4) (1976) 695–719, doi:10.1017/S0022112076002012.

[7] T.H. Kuehn, R.J. Goldstein, An experimental study of natural convection heat transfer in concentric and eccentric horizontal cylindrical annuli, J.Heat Transf. 100 (4) (1978) 635–640, doi:10.1115/1.3450869.

[8] J.-S. Yoo, Prandtl number effect on bifurcation and dual solutions in natural convection in a horizontal annulus, Int. J.Heat Mass Transf. 42 (17) (1999) 3279–3290, doi:10.1016/S0017-9310(98)00384-6.

[9] J. Mizushima, S. Hayashi, Exchange of instability modes for natural convection in a narrow horizontal annulus, Phys. Fluids 13 (1) (2001) 99–106, doi:10.1063/1.1329649.

[10] J. Mizushima, S. Hayashi, T. Adachi, Transitions of natural convection in a horizontal annulus, Int. J.Heat Mass Transf. 44 (6) (2001) 1249–1257, doi:10.1016/S0017-9310(00)00188-5.

[11] S. Xin, P. Le Quéré, Linear stability analyses of natural convection flows in a differentially heated square cavity with conducting horizontal walls, Phys. Fluids 13 (9) (2001) 2529–2542, doi:10.1063/1.1388054.

[12] I. Mercader, O. Batiste, L. Ramírez-Piscina, X. Ruiz, S. Rüdiger, J. Casademunt, Bifurcations and chaos in single-roll natural convection with low Prandtl number, Phys. Fluids 17 (10) (2005) 104108, doi:10.1063/1.2107907.

[13] T. Tayebi, A.J. Chamkha, Natural convection enhancement in an eccentric horizontal cylindrical annulus using hybrid nanofluids, Numer. Heat Transf. Part A 71 (11) (2017) 1159–1173, doi:10.1080/10407782.2017.1337990.

[14] T. Tayebi, H.F. Öztop, A.J. Chamkha, MHD natural convection of a CNT-based nanofluid-filled annular circular enclosure with inner heat-generating solid cylinder, Eur. Phys. J. Plus 136 (2) (2021) 150, doi:10.1140/epjp/s13360-021-01106-7.

[15] R.E. Powe, C.T. Carley, E.H. Bishop, Free convective flow patterns in cylindrical annuli, J.Heat Transf. 91 (3) (1969) 310–314, doi:10.1115/1.3580158.

[16] M.P. Dyko, K. Vafai, A.K. Motjabi, A numerical and experimental investigation of stability of natural convective flows within a horizontal annulus, J. Fluid Mech. 381 (1999) 27–61, doi:10.1017/S0022112098002948.

[17] R.J.A. Janssen, R.A.W.M. Henkes, Instabilities in three-dimensional differentially-heated cavities with adiabatic horizontal walls, Phys. Fluids 8 (1) (1996) 62–74, doi:10.1063/1.868814.

[18] G. Petrone, E. Chénier, G. Lauriat, Stability analysis of natural convective flows in horizontal annuli: effects of the axial and radial aspect ratios, Phys. Fluids 18 (10) (2006) 104107, doi:10.1063/1.2364027.

[19] D. Angeli, G. Barozzi, M. Collins, O. Kamiyo, A critical review of buoyancy-induced flow transitions in horizontal annuli, Int. J. Therm. Sci. 49 (12) (2010) 2231–2241, doi:10.1016/j.ijthermalsci.2010.08.002.

[20] L. Soucasse, P. Rivière, A. Soufiani, S. Xin, P. Le Quéré, Transitional regimes of natural convection in a differentially heated cubical cavity under the effects

of wall and molecular gas radiation, Phys. Fluids 26 (2) (2014) 024105, doi:10.1063/1.4864265.

[21] J.M. Lopez, F. Marques, Instability of plumes driven by localized heating, J. Fluid Mech. 736 (2013) 616–640, doi:10.1017/jfm.2013.537.

[22] W. Coenen, L. Lesshafft, X. Garnaud, A. Sevilla, Global instability of low-density jets, J. Fluid Mech. 820 (2017) 187–207, doi:10.1017/jfm.2017.203.

[23] D. Ho-Minh, D. Mai, T. Cong Cong, A Galerkin-RBF approach for the stream-function-vorticity-temperature formulation of natural convection in 2D enclosured domains, CMES 44 (2009).

[24] C. Shu, Application of differential quadrature method to simulate natural convection in a concentric annulus, Int. J. Numer. MethodsFluids 30 (8) (1999) 977–993, doi:10.1002/(SICI)1097-0363(19990830)30:8<977::AID-FLD873>3.0.CO;2-J.

[25] J.D. Chung, C.-J. Kim, H. Yoo, J.S. Lee, Numerical investigation on the bifurcative natural convection in a horizontal concentric annulus, Numer. Heat Transf. Part A 36 (3) (1999) 291–307, doi:10.1080/104077899274778.

[26] F. Selimefendigil, H.F. Öztop, Conjugate natural convection in a nanofluid filled partitioned horizontal annulus formed by two isothermal cylinder surfaces under magnetic field, Int. J.Heat Mass Transf. 108 (2017) 156–171, doi:10.1016/j.ijheatmasstransfer.2016.11.080.

[27] K. Kahveci, Stability of unsteady mixed convection in a horizontal concentric annulus, J. Appl. Fluid Mech. 9 (5) (2016) 2141–2147.

[28] J. Wu, P. Traoré, M. Zhang, A.T. Pérez, P.A. Váquez, Charge injection enhanced natural convection heat transfer in horizontal concentric annuli filled with a dielectric liquid, Int. J.Heat Mass Transf. 92 (2016) 139–148, doi:10.1016/j.ijheatmasstransfer.2015.08.088.

[29] Y. Zhao, B. Zhang, A high-order characteristics upwind FV method for incompressible flow and heat transfer simulation on unstructured grids, Comput. Methods in Appl. Mech.Eng. 190 (5–7) (2000) 733–756.

[30] E. Abu-Nada, Effects of variable viscosity and thermal conductivity of Al_2O_3-water nanofluid on heat transfer enhancement in natural convection, Int. J. Heat Fluid Flow 30 (4) (2009) 679–690, doi:10.1016/j.ijheatfluidflow.2009.02.003.

[31] K. Luo, H.-L. Yi, H.-P. Tan, Eccentricity effect on bifurcation and dual solutions in transient natural convection in a horizontal annulus, Int. J. Therm. Sci. 89 (2015) 283–293, doi:10.1016/j.ijthermalsci.2014.11.020.

[32] Y. Cao, Y. Zhang, Investigation on the natural convection in horizontal concentric annulus using the variable property-based lattice Boltzmann flux solver, Int. J.Heat Mass Transf. 111 (2017) 1260–1271, doi:10.1016/j.ijheatmasstransfer.2017.04.071.

[33] C. Shu, H. Xue, Y. Zhu, Numerical study of natural convection in an eccentric annulus between a square outer cylinder and a circular inner cylinder using DQ method, Int. J.Heat Mass Transf. 44 (17) (2001) 3321–3333, doi:10.1016/S0017-9310(00)00357-4.

[34] M. Sheikholeslami, M. Gorji-Bandpy, D. Ganji, S. Soleimani, Effect of a magnetic field on natural convection in an inclined half-annulus enclosure filled with Cu-water nanofluid using CVFEM, Adv. Powder Technol. 24 (6) (2013) 980–991, doi:10.1016/j.apt.2013.01.012.

[35] Y. Liang, Z. Sun, G. Xi, L. Liu, Numerical models for heat conduction and natural convection with symmetry boundary condition based on particle method, Int. J.Heat Mass Transf. 88 (2015) 433–444, doi:10.1016/j.ijheatmasstransfer.2015.04.105.

[36] X. Yang, S.-C. Kong, Numerical study of natural convection in a horizontal concentric annulus using smoothed particle hydrodynamics, Eng. Anal. Boundary Ele. 102 (2019) 11–20, doi:10.1016/j.enganabound.2019.02.007.

[37] J.A. Weideman, S.C. Reddy, A matlab differentiation matrix suite, ACM Trans. Math. Softw. 26 (4) (2000) 465–519, doi:10.1145/365723.365727.

[38] M. Napolitano, G. Pascazio, L. Quartapelle, A review of vorticity conditions in the numerical solution of the $\zeta - \psi$ equations, Comput. Fluids 28 (2) (1999) 139–185, doi:10.1016/S0045-7930(98)00024-3.

[39] U.M. Ascher, L.R. Petzold, Computer Methods for Ordinary Differential Equations and Differential-Algebraic Equations, first ed., Society for Industrial and Applied Mathematics, USA, 1998.

[40] J.-S. Yoo, Dual steady solutions in natural convection between horizontal concentric cylinders, Int. J. Heat Fluid Flow 17 (6) (1996) 587–593, doi:10.1016/S0142-727X(96)00064-1.

[41] K.K. Bharadwaj, D. Das, Puffing in planar buoyant plumes: BiGlobal instability analysis and experiments, J. Fluid Mech. 863 (2019) 817–849, doi:10.1017/jfm.2018.1022.

[42] O. Tammisola, F. Lundell, P. Schlatter, A. Wehrfritz, L.D. Södeberg, Global linear and nonlinear stability of viscous confined plane wakes with co-flow, J. Fluid Mech. 675 (2011) 397–434, doi:10.1017/jfm.2011.24.